Production of nanohole/nanodot patterns on Si(001) by ion beam sputtering with simultaneous metal incorporation

2009 J. Phys.: Condens. Matter 21 224009

(http://iopscience.iop.org/0953-8984/21/22/224009)

J. Phys.: Condens. Matter **21** (2009) 224009 (13pp) doi:10.1088/0953-8984/21/22/224009

Production of nanohole/nanodot patterns on Si(001) by ion beam sputtering with simultaneous metal incorporation

J A Sánchez-García[1], R Gago[1,2], R Caillard[1], A Redondo-Cubero[2], J A Martin-Gago[1,3], F J Palomares[1], M Fernández[1] and L Vázquez[1]

[1] Instituto de Ciencia de Materiales de Madrid, Consejo Superior de Investigaciones Científicas, E-28049 Madrid, Spain
[2] Centro de Micro-Análisis de Materiales, Universidad Autónoma de Madrid, E-28049 Madrid, Spain
[3] Centro de Astrobiología (CSIC-INTA), Carretera de Torrejón a Ajalvir, km 4, 28850 Torrejón de Ardoz, Madrid, Spain

E-mail: lvb@icmm.csic.es (L Vázquez)

Received 11 February 2009
Published 12 May 2009
Online at stacks.iop.org/JPhysCM/21/224009

Abstract

We have established the conditions for which nanohole and nanodot patterns are produced on Si(001) surfaces by 1 keV Ar^+ ion beam sputtering (IBS) at normal incidence with an alternating cold cathode ion source (ACC-IS). Nanohole patterns are produced within a narrow IBS window for low ion fluxes ($<100\ \mu A\ cm^{-2}$) and relatively low ion fluences ($<10^{18}$ ions cm^{-2}) whereas nanodot morphologies are produced above this window. The nanohole pattern is not stable after prolonged irradiation since it evolves to a nanodot morphology. Rutherford backscattering spectrometry (RBS) measurements show that nanohole patterns are produced when the metal content on the irradiated surfaces is higher (within $(2.5–3.5 \times 10^{15})$ atoms cm^{-2}) than in the case of nanodots ($<2.5 \times 10^{15}$ atoms cm^{-2}). The different metal content is related to the ACC-IS operation, since the set-up provides simultaneous incorporation of Fe and Mo on the target surface from the erosion of the cathodes and sample holder, respectively. The role of metal incorporation on pattern selectivity has been corroborated qualitatively by extending the results obtained with the ACC-IS to a standard Kaufman-type source. In order to gain further information on the metal effects, chemical analysis of the surface has been performed to complement the compositional RBS results, showing for the first time the relevant participation of metal silicides. Further outlook and a discussion regarding the role of metal incorporation are also given.

(Some figures in this article are in colour only in the electronic version)

1. Introduction

As this special issue shows, ion beam sputtering (IBS) has become an attractive route by which to spontaneously induce self-organized nanostructures on different surfaces. This technique has proved to be suitable for producing a pattern, mainly consisting of either rippled or dotted nanostructures, on single-crystal, polycrystalline and amorphous surfaces [1, 2]. This pattern is induced in a very short time (a few minutes) and over relatively large areas.

The studies of IBS pattern formation by different groups during the last few years have contributed to a deepening of our knowledge about its underlying physical mechanisms [3–5]. This special issue confirms the evident progress achieved in the understanding and experimental control of IBS nanopatterning. However, at the same time, it shows clearly that there are still open issues concerning IBS surface patterning from the theoretical and experimental points of view. In the first case, although new models have been proposed [5], it is not clear if some additional physical mechanisms should also

be taken into account. Among these, we can highlight the possible role played by surface stress and by the existence of a viscous surface layer. From the experimental point of view, the open issues refer mainly to the reproducibility of IBS nanopatterning, the possibility of tuning the pattern morphologies, and the eventual enhancement (and control) of the pattern ordering. Besides, there is the important issue of the discrepancy between the theoretically predicted universal character of IBS nanopatterning and the diversity of patterns obtained experimentally on different materials (see, for example, other articles included in this special issue). This discrepancy can be partially attributed to the specific characteristics of each experimental system. In this sense, it would be important to determine the extent of the influence of the ion gun employed in the IBS process on the final pattern morphology [6]. Other issue refers to the problems usually found in patterning single-element semiconductor surfaces, particularly silicon [7, 8]. This contrasts with the relatively easy patterning of compound semiconductors, such as GaSb, where preferential sputtering effects of one species could be relevant [9]. Although the successful production of nanodot patterns by IBS has been reported on silicon surfaces [10, 11], the lack of reproducibility has motivated some additional considerations such as the need for surface impurities, typically metals, to effectively induce such patterns. This possibility was firstly proposed by Ozaydin *et al* [12]. The authors claimed that Mo-seeding on the surface was a necessary condition to induce a nanodot pattern on Si(100) under normal ion irradiation with a 1 keV Ar^+ ion beam. It was suggested that Mo induced a certain surface roughness and triggered preferential sputtering effects, which may be required to initiate the patterning process of elemental semiconductors. In this sense, Shenoy *et al* [13] have also recently highlighted the role played by preferential sputtering in modulating the surface composition with respect to the topography.

Recently, Sanchez-García *et al* [14] addressed the role of incorporation of Fe and Mo during IBS patterning of Si(001) to tune the surface morphology from nanohole to nanodot patterns. It was found that the final pattern morphology could be selectively produced during bombardment of Si(001) with a 1 keV Ar^+ ion beam at normal incidence in correlation with the residual metal content on the surface after irradiation. The irradiations were realized with an alternating cold cathode ion source (ACC-IS) [15]. Thus, patterned surfaces with nanohole morphologies exhibited a metal content twice that found on the nanodot structured surfaces, as derived from Rutherford backscattering spectrometry (RBS). From a practical point of view, these nanohole patterns could be used as templates for selective surface growth with the aim of patterned surface functionalization or the achievement of confined nanostructures. Selective growth on nanostructured substrates [16–19] can have important applications for fast electronic devices [20] and high-density data storage [21].

From the above, the relevance of simultaneous metal incorporation to the production of surface patterns by IBS is clear, especially for silicon surfaces and in the case of nanohole morphologies. However, the lack of systematic chemical characterizations of the irradiated surfaces leaves open the question of whether metal incorporation (and beyond which threshold value) is necessary to pattern single-element semiconductor surfaces. In any case, for such systems where metal incorporation does seem to play a role, the mechanisms involved are still not clear enough. For example, nanodot patterns produced with a Kaufman ion source [10] present non-negligible Fe incorporation, although the content is much lower than that achieved with the ACC-IS [14] or reported by other groups [12]. All these results indicate the importance of chemical characterization of the IBS patterned surfaces to determine the (un)intentional metal incorporation during IBS patterning. Moreover, it is worth noting that to date, whenever such characterization has been addressed, it has not been possible to assess the presence of metal silicides at the patterned surface [12, 14]. Their existence would alter the actual surface local sputtering yield and, therefore, the local surface morphology.

The main aim of this work is to further explore the effect of simultaneous metal incorporation on IBS surface patterning and to deepen our understanding of the mechanisms involved in such processes. In our previous study [14], we established the relationship between the surface morphology and the metal content as a function of the ion flux for fixed fluence conditions (i.e. 4×10^{17} ions cm^{-2}). Therefore, that study was confined to a relatively narrow experimental IBS parameter window. A first goal of this work consists in assessing whether that finding still holds after a more extensive study. Accordingly, we have extended this window and explored systematically the role of simultaneous Fe/Mo incorporation on the production of nanohole and nanodot patterns. From this analysis, we can further verify the previously reported correlation between the total metal content and pattern morphology. Moreover, based on the acquired knowledge, we have been able to achieve the formation of nanohole patterns by IBS with a Kaufman source by indirectly tuning the amount of metal incorporation with this type of ion gun. Finally, we have performed a comparative analysis of surfaces with both nanohole and nanodot patterns by x-ray photoelectron spectroscopy (XPS) and Auger electron spectroscopy (AES). These techniques provide complementary compositional analysis to RBS with a higher depth resolution, and allow us to investigate the chemical state of the constituents. Complementarily, AES gives valuable in-depth information. In this way, we have been able to determine that metal atoms are forming silicide bonds and that metals are buried deeper for the nanohole morphologies. The formation of silicides, reported for the first time, and the metal distribution can imply relevant modifications to the local sputtering yield giving place to the different morphologies.

2. Experimental details

2.1. Sample preparation by IBS

Single-crystal n-type Si(001) targets (Sb doped, 8–20 $\times$ 10^{-3} Ω cm) were bombarded with 1 keV Ar^+ ions at normal incidence in a high vacuum chamber with a base pressure of 4×10^{-7} mbar. For most irradiations, the ion beam was extracted from an ACC-IS (Jenion GmbH [15])

under experimental conditions described elsewhere [14]. The targets were bombarded with current densities (J) between 40 and 340 μA cm^{-2} and ion fluences up to $\sim 4 \times 10^{18}$ ions cm^{-2}. Eventually, IBS experiments were performed with a commercial CSC Kaufman-type ion gun (Veeco©) with a 3 cm beam diameter under similar working conditions. In all experiments, the target current density was adjusted prior to the IBS process with a Faraday Cup located on a movable shutter covering the target. The obtained values were further checked by calibration of the erosion rate, as derived from profilometry. For this purpose, the step created between exposed and masked parts of the sample was measured with a Dektak 150 (Veeco©) mechanical profilometer. For masking, we used Mo (ACC-IS) or Fe–Mo (Kaufman) foils with an inner hole of 18 mm or a diameter of 10 mm, respectively. These masks are used to fix the target and, simultaneously, to control the metal incorporation rate.

2.2. Morphological characterization of the target surface after IBS

The resulting surface morphology was imaged *ex situ* by tapping mode atomic force microscopy (AFM) with Nanoscope IIIa equipment (Veeco©). Silicon cantilevers with a nominal radius of 10 nm were employed. In order to characterize the pattern wavelength we derived the power spectral density (PSD) from the AFM images [14]. Another useful parameter for characterizing AFM morphologies is the surface skewness, S, which is a measure of the vertical asymmetry of the surface [22] and, hence, sensitive to the presence of protruding or hollow features. If $\langle h(\mathbf{r})\rangle$ is the average height of a surface, S is defined as $\langle h(\mathbf{r}) - \langle h(\mathbf{r})\rangle\rangle^3 / w^3$, where w is the root mean square surface roughness and here the angular brackets denote spatial averaging. In our case, PSD functions, w, S and $\langle h(\mathbf{r})\rangle$ values are obtained directly by the software of the AFM equipment.

2.3. Compositional and chemical analysis of the target surface after IBS

The residual composition of the irradiated surfaces was determined routinely by means of RBS with a 1 MeV He$^+$ probing beam. The spectra were acquired under random geometry with a Si solid-state detector located at a scattering angle of 170°. Additionally, XPS analysis was carried out in selected samples using a hemispherical electron analyser with a Mg Kα x-ray source operating in an ultra high vacuum chamber with a base pressure in the 1×10^{-9} mbar range. The measurements were performed before and after gentle 5 keV Ar$^+$ sputter cleaning to remove spurious signal from surface contamination. Compositional analysis by XPS was performed by assuming a homogeneous distribution of Fe and Mo at the near surface region and using tabulated atomic sensitivity factors (0.27, 3.00 and 2.75 for Si 2p, Mo 3d and Fe 2p, respectively) [23]. In addition, high-resolution XPS data were acquired with a SPECS Phoibos 150 spectrometer with a hemispherical analyser using monochromatic Al Kα radiation. The spectra were recorded at normal emission take-off angle, using an energy step of 0.05 eV and a pass-energy of 10 eV, which provides an overall energy resolution of ~0.40 eV. Finally, AES compositional profiles were recorded by sequential sputtering and measurement cycles with a JEOL system (JAMP-10S). The spectra were recorded with a 5 keV electron probing beam of ~0.1 mm diameter at normal incidence. For depth profiling experiments, the samples were bombarded with 2 keV Ar$^+$ at an angle of incidence of 55°. The quantitative computations were made from the measurements of the intensities of the Si LVV(92 eV), Mo MNN(184 eV) and Fe LMM (598, 651 and 703 eV) Auger lines with a low attenuation length (~0.5 nm).

3. Results and discussion

3.1. Dependence of pattern morphology on IBS conditions with an ACC-IS

Figure 1 shows the resulting surface topography after irradiation for increasing J values for a constant ion fluence of $\sim 6 \times 10^{17}$ ions cm^{-2}. Qualitatively, the results are analogous to those reported previously [14] for a lower ion fluence, where roughly five different surface topographies are distinguished for increasing J values: (i) *flat surfaces* with a roughness similar to that of the bare Si(001) target (not shown); (ii) *scattered nanohole structures* (see figure 1(a)), 15–35 nm wide, over flat hole-free plateau regions; (iii) *dense nanohole structures* with an average diameter of ~22 nm (see figure 1(b)) (note that the nanohole dimensions could be underestimated because of tip convolution effects); (iv) a *mixed pattern* (see figure 1(c)) where both nanohole and nanodot structured morphologies coexist; and (v) a *dense nanodot pattern* (see figure 1(d)). The latter pattern is similar to those reported previously with a Kaufman-type ion gun [10]. As shown previously [14], both dense nanohole and nanodot patterns can be quite similar in terms of homogeneity, surface roughness, wavelength and short-range order. In particular, the insets of figures 1(b) and (d) show that both dense patterns display hexagonal short-range ordering.

In order to gain a deeper understanding of nanohole/nanodot pattern formation, we have extended the previous study in terms of ion flux and fluence. For this purpose, samples irradiated in a wide range of ion currents and sputtering times were characterized by AFM and their topography ascribed to either flat (□), nanohole (○), mixed (■) or nanodot (●) morphologies following the criteria established earlier [14] from the skewness of the AFM images. The results from this analysis are shown in figure 2. Visual inspection of the symbol distribution in figure 2 clearly leads to the following conclusions: (i) nanohole structures are only formed for low J values and they are never observed for $J > 110$ μA cm^{-2}; (ii) in contrast, nanodot patterns are induced at higher J conditions; and (iii) nanodot structures are always produced, for a given J, above a certain fluence onset. In any case, this plot indicates that the most likely pattern to be found in IBS experiments with simultaneous metal incorporation would be the nanodot morphology, which is consistent with previous reports by Ozaydin *et al* [12, 24]. In contrast, nanohole patterns are formed within a narrow window, mostly for low ion fluxes.

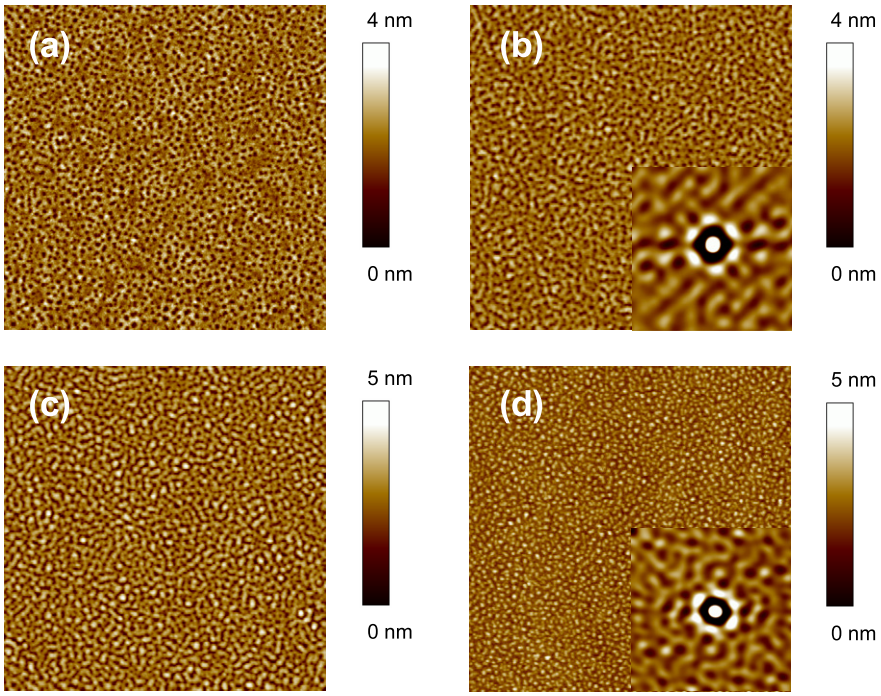

Figure 1. $2 \times 2\ \mu m^2$ AFM images showing the morphology of Si(001) surfaces irradiated with an ACC-IS under normal incidence with 1 keV Ar^+ for an ion fluence of 6×10^{17} ions cm^{-2} at: (a) $J = 40\ \mu A\ cm^{-2}$ (scattered nanoholes), (b) $J = 55\ \mu A\ cm^{-2}$ (nanohole pattern); (c) $J = 90\ \mu A\ cm^{-2}$ (mixed pattern); and (d) $J = 250\ \mu A\ cm^{-2}$ (nanodot pattern). The insets of (b) and (d) show the corresponding auto-correlation functions taken on $400 \times 400\ nm^2$ regions.

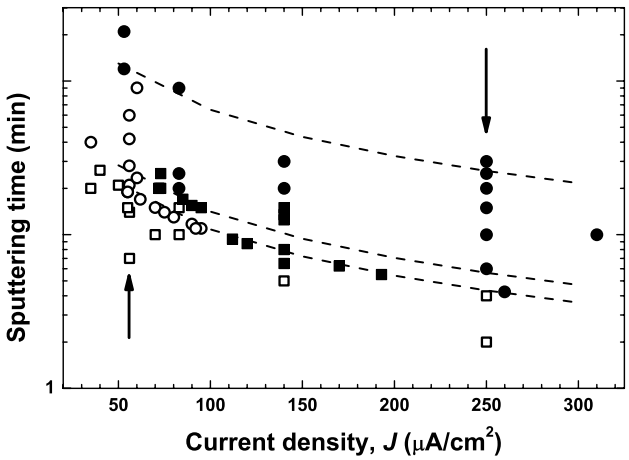

Figure 2. Mapping of the surface morphology resulting from IBS of Si(001) for different J and sputtering times. The experimental error in J is $\pm 10\ \mu A\ cm^{-2}$. The different morphologies are displayed with characteristic symbols: flat (□), nanohole (○), mixed (■) and nanodot (●). The dashed curves indicate constant ion fluence conditions, namely 2.5×10^{18}, 5.8×10^{17} and 4×10^{17} ions cm^{-2} from top to bottom. The arrows indicate the temporal series at low and high ion flux discussed in detail in the text.

Regarding the pattern dependence on J for different ion fluence values, the morphological evolution presents some peculiarities worth mentioning. From the dashed lines in figure 2, the pattern morphologies for ion fluences of 2.5×10^{18} (top), 5.8×10^{17} (middle) and 4×10^{17} (bottom) ions cm^{-2} can be followed. For the lowest ion fluence condition, the surface morphology evolves with J from a flat surface to a nanohole–mixed–nanodot pattern sequence, as described in [14]. For the middle ion fluence, the pattern sequence is the same although the thresholds shift to lower J values. Finally, for the highest fluence, the pattern morphology does not change and nanodot morphologies are produced already from the lowest J value sampled.

3.2. Nanodot/nanohole pattern dynamics during IBS with an ACC-IS

As shown schematically in figure 2, at a constant ion current density there is a pattern transition for increasing irradiation times. To follow this change, we have studied the evolution for low and high ion fluxes (marked by arrows in figure 2), namely 55 and 250 $\mu A\ cm^{-2}$. The AFM images for selected samples irradiated under these conditions are shown in figure 3. In addition, for both ion current densities, figure 4 shows the PSD curves (left panel) and a detailed quantitative analysis (right panel) of the AFM images.

For conditions of low J ($55\ \mu A\ cm^{-2}$), the target surface remains flat for irradiation times below 15 min. After ~20 min, a dense nanohole pattern is observed, as shown in figure 3(a). The appearance of a pattern leads to a clear peak in the PSD curve at $k_{max} = 1/\lambda$ (figure 4(a)). This type of structure is still formed for a relatively large temporal window (up to 90 min), but as the irradiation time increases the nanohole structures become scarcer and more scattered over the surface (figure 3(b)). Accordingly, this evolution leads to larger λ values for longer irradiations times, as evidenced by the

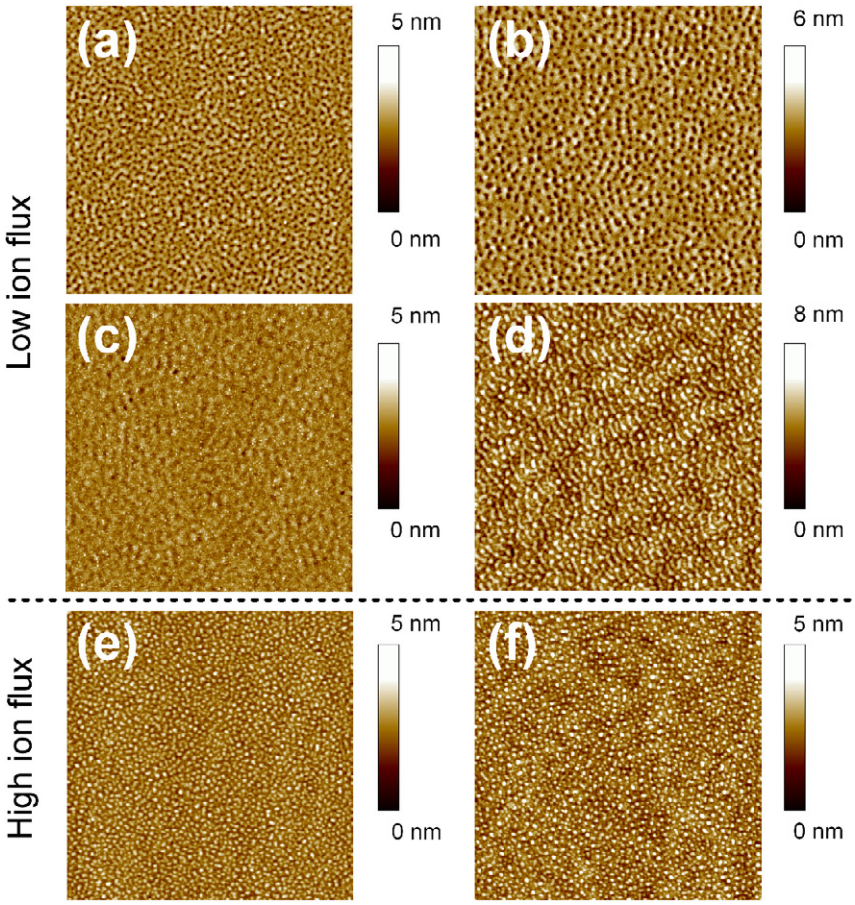

Figure 3. $2 \times 2\ \mu m^2$ AFM images showing the change in morphology for a Si(001) surface irradiated under normal incidence by a 1 keV Ar^+ ion beam for an ion flux of 55 μA cm^{-2} (a–d) and 250 μA cm^{-2} (e, f) for sputtering times of: (a) 28 min; (b) 90 min; (c) 120 min; (d) 210 min; (e) 10 min; (f) 30 min.

gradual shift towards smaller k values with time of the PSD peak in figure 4(a). In fact, the increase of λ with the ion fluence for this nanohole regime follows an approximate law as $\lambda \sim t^{0.1}$ (figure 4(c)). After 2 h of irradiation the surface morphology becomes abruptly smoother (see figures 3(c) and 4(d)) since the nanohole structures have completely disappeared. Finally, for the longest irradiation time employed (210 min) a clear nanodot structure develops (figure 3(d)) with $\lambda \sim 59$ nm (figure 4(c)). The surface roughness increases as $t^{0.7}$ until the abrupt smoothing, occurring after 2 h of irradiation (figure 4(d)). Afterwards, with the development of the nanodot pattern, the roughness increases again. The evolution of surface morphology with ion fluence can be followed in figure 4(e), where the skewness from the AFM images is plotted as a function of ion fluence. The measured skewness becomes clearly negative ($S < -0.2$), consistent with the observed nanohole morphology, for ion fluences close to 10^{18} ions cm^{-2}. After this value, the skewness increases up to $S \sim 0.3$ for the longest irradiation times, indicating that transition to the nanodot pattern takes place. This plot also shows the unstable character of the nanohole pattern, since it evolves to a nanodot pattern (positive S values) with fluence.

For conditions of high J (250 μA cm^{-2}), a clear nanodot pattern (figure 3(e)) is already formed after just a few minutes of irradiation ($t > 6$). The pattern formation leads to a clear peak in the corresponding PSD curve (figure 4(b)). This pattern is stable upon further irradiation up to the highest ion fluence sampled (figure 3(f)). As the ion fluence increases, the peak of the PSD curve shifts to lower k values, indicating that the pattern undergoes a coarsening process, $\lambda \sim t^{0.17}$, faster than in the low J case (figure 4(c)). The surface roughens, following a similar behaviour to that found at low J (figure 4(d)) but, for higher ion fluences, roughening takes place much more slowly. Finally, in contrast to the low J case, figure 4(e) shows how the irradiated surface displays a clear positive S value for practically the whole ion fluence range sampled corresponding to the observed nanodot pattern morphology. It is also interesting to note that ordering in the nanodot patterns (as derived from the PSD peak width) produced at low J (i.e. slower dynamics) attains a higher asymptotic value than at high J. A similar trend was also reported in the dynamics of nanodot pattern formation with a Kaufman ion source [25, 26].

3.3. Effect of target temperature on nanohole pattern formation

Theoretically, the formation and evolution of surface nanostructures by IBS is described from the balance between smoothing processes and an instability induced

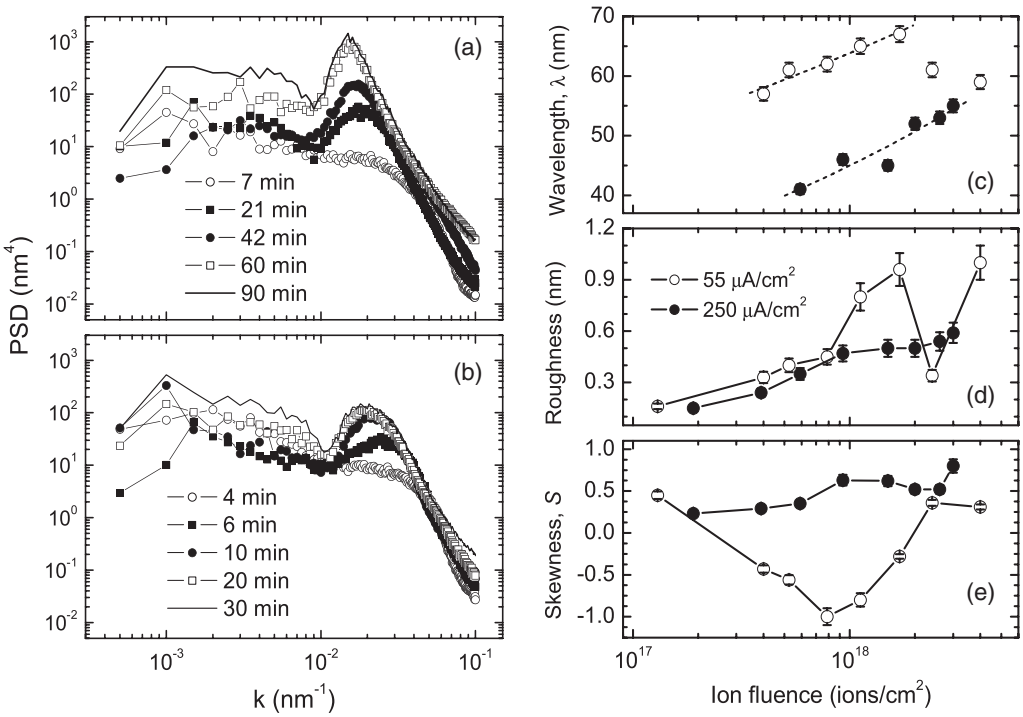

Figure 4. PSD functions of the samples irradiated for different times at 55 μA cm^{-2} (a) and 250 μA cm^{-2} (b). Change of the pattern wavelength (c), surface roughness (d) and surface skewness (e) with ion fluence for samples irradiated at 55 μA cm^{-2} (○) at 250 μA cm^{-2} (▲).

by the dependence of the sputtering yield on the surface curvature [1, 2]. Therefore, among the relevant process parameters, target temperature (T) during IBS can play a significant role in the nanostructuring process by governing surface diffusion processes. The effect of T on the formation of nanodots by IBS was addressed in a previous communication [27], resulting in an interesting behaviour not accounted for by the current theoretical models. Here, in order to deepen our understanding of the operating mechanisms governing nanohole pattern formation, we have performed a similar study and explored the dependence of nanohole morphology on the target temperature. Thus, we performed IBS experiments varying the temperature under the conditions described above where nanohole patterns are formed without intentional heating ($J = 75$ μA cm^{-2} and an ion fluence of 7×10^{17} ions cm^{-2}).

The morphological evolution for increasing target T is followed in the AFM images (figure 5) and their corresponding analysis (figure 6). The AFM images show that nanohole structures are only found when IBS takes place at 290 K and 333 K (figures 5(a) and (b), respectively). In both cases, no intentional (i.e. external) heating was applied. The former temperature corresponds to experiments with a water-cooled holder, whereas the latter value was obtained during irradiation with the cooling system off. In this T range (<350 K), the nanohole pattern becomes denser at higher T (figures 5(a) and (b) and 6(a) and (b)). For higher T the nanohole pattern disappears, leading to a network-like morphology in which nanoholes and nanodots can be found (figures 5(c) and (d)). However, the PSD curves (figure 6(a)) still display a clear peak, indicating that the roughness has a preferred correlation length. As shown in figures 6(a) and (b), the dominant wavelength continues to decrease with T (shift of the PSD peak to higher wavenumbers) for the whole range sampled but at a smaller rate than in the initial nanohole regime. In contrast, the surface roughness (see figure 6(c)) increases with T until a maximum is reached at 433–483 K. For $T > 483$ K, the roughness decreases continuously.

In figure 6(a), together with the experimental results, we show the theoretical curve (dashed line) expected for a surface whose morphology is determined by linear thermally activated surface diffusion processes [28]. This behaviour is consistent with that observed for the PSD curves at high k values, that is, for short length scales (smaller than λ). At the highest temperature, the surface becomes smoother (figure 6(c)) and the relative height of the peak of the corresponding PSD (figure 6(b)) is appreciably smaller than at lower temperatures, indicating that the surface instability is smoothed out due to the surface diffusion relaxation processes. These findings show that nanohole patterns are not formed when the target temperature is increased beyond ∼350 K. This observation is consistent with the observed production of nanoholes at low J and ion fluence values, where the increase in sample temperature due to ion impingement is expected to be below this threshold.

3.4. Compositional analysis of the irradiated surfaces by RBS

We have characterized by RBS a representative set of samples in terms of morphology from the mapping displayed in figure 2. Figure 7 displays the total metal content and

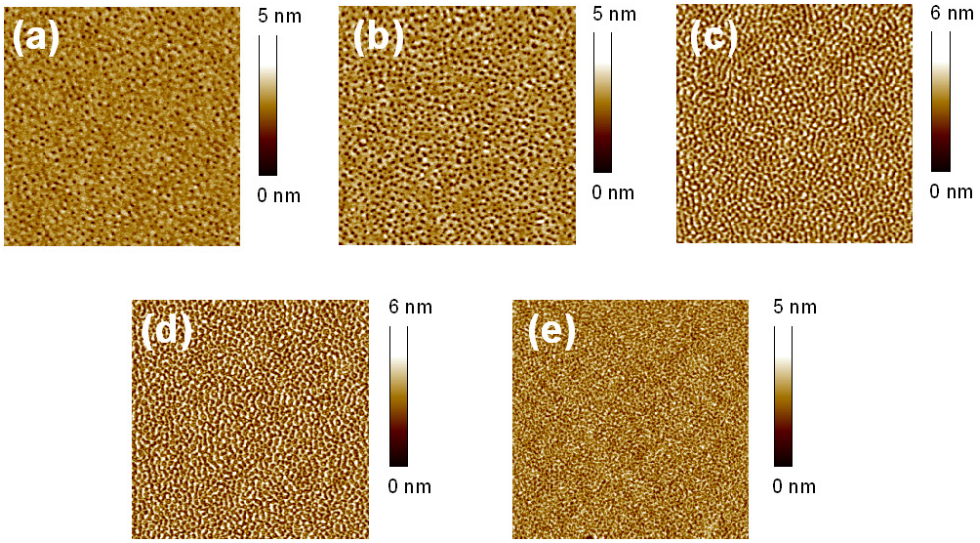

Figure 5. $2 \times 2\ \mu m^2$ AFM images showing the change in morphology for a Si(001) surface irradiated at normal incidence by a 1 keV Ar^+ ion beam for an ion flux of 75 μA cm^{-2} and an ion fluence of 7×10^{17} ions cm^{-2} at: (a) 290 K, (b) 333 K, (c) 383 K, (d) 573 K and (e) 710 K.

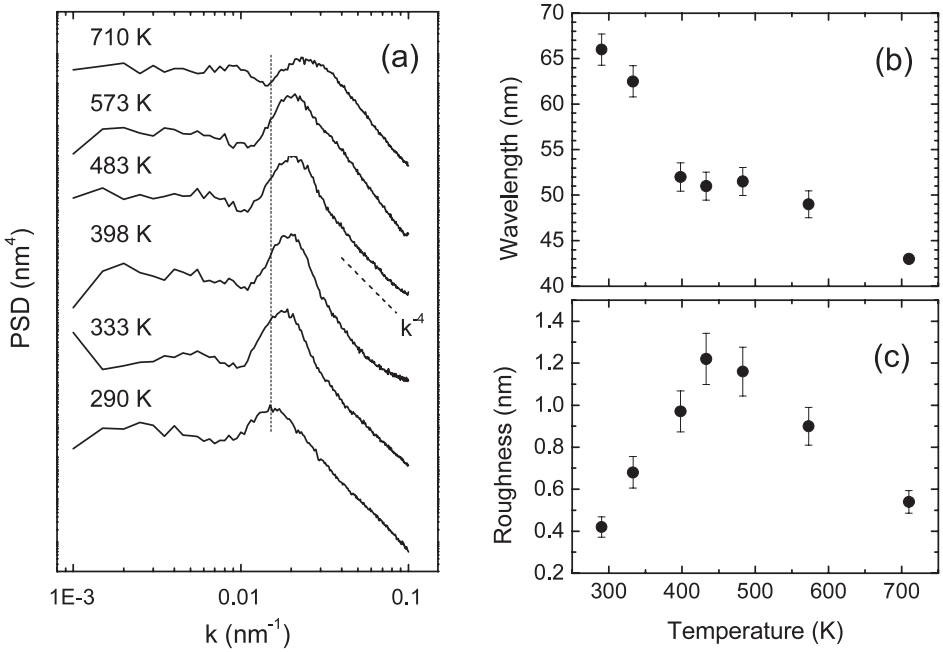

Figure 6. Left panel: (a) PSD functions for samples irradiated at 75 μA cm^{-2} at substrate temperatures of 290, 333, 398, 483, 573 and 710 K. The dashed line indicates the behaviours expected for a PSD $\propto k^{-4}$ dependence. The vertical line indicates the position of the peak for the lowest T condition. For clarity the PSD curves have been artificially shifted vertically. Right panel: change of the (b) pattern wavelength, λ, and (c) surface roughness, w, with T.

the Fe/Mo content ratio, respectively, as a function of surface skewness, S. In such a representation, the nanohole morphology has to be found at the left part of the x-axis (i.e. $S < -0.2$) whereas the nanodot region lies at the right x-axis region (i.e. $S > 0.2$). The symbols also help to clearly identify the surface morphology (see caption for more details). Note that we have plotted the areal density of atoms (atoms cm^{-2}) extracted directly by RBS.

Clearly, the symbol distribution in figure 7(a) shows that nanohole morphologies are located, regardless of J and fluence, mainly at the top left part of the graph while the nanodot patterns appear mostly at the right bottom region of the plot. This distribution indicates that nanohole structures appear for total metal contents in the (2.5–3.7) $\times$ 10^{15} atoms cm^{-2} range whereas nanodot patterns are produced for total metal contents lower than $\sim 2.5 \times 10^{15}$ atoms cm^{-2}. On the contrary, figure 7(b) indicates that there is no correlation between the Fe/Mo ratio and the type of pattern, since nanohole morphologies can correspond to both low ($\sim$1) and high ($\sim$6) Fe/Mo ratios. Therefore, these findings corroborate our experimental conclusion reported earlier [14].

As pointed out in figure 3, the pattern dynamics during IBS shows a pattern onset inversely proportional to J and, interestingly, a morphological transition from nanoholes to

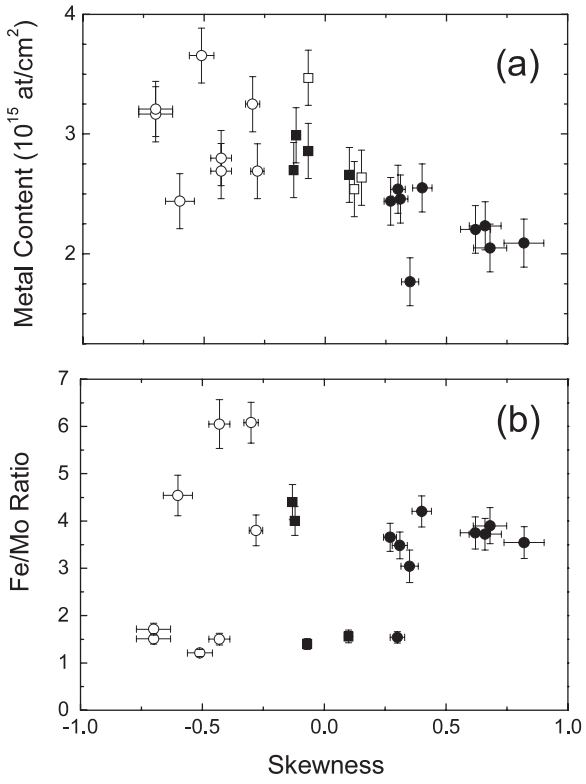

Figure 7. Total metal content (a) and Fe/Mo ratio (b) measured by RBS as a function of the surface skewness from the AFM images. The symbols correspond to the following surface morphologies: flat (□), nanohole (○), mixed (■) and nanodot (●).

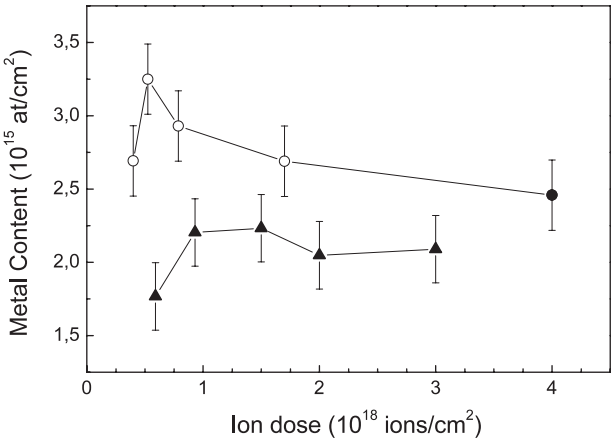

Figure 8. Total metal content measured by RBS as a function of ion fluence for targets irradiated at 55 μA cm^{-2} (top curve) and 250 μA cm^{-2} (bottom curve). Open and filled symbols correspond to nanohole and nanodot morphologies, respectively.

nanodots for low J values. A possible correlation between the metal content and the surface morphology in these samples may give some hints about this pattern transition and, especially, about nanohole formation. For this purpose, we have analysed the composition of samples produced at 55 and 250 μA cm^{-2} for different fluences, as shown in figure 8. Open symbols refer to nanohole structures whereas filled ones correspond to nanodot patterns in accordance with figure 3. The comparison of both trends yields that, for similar ion fluences, the metal content on the surface is always higher for lower J. In the ACC-IS system, Fe and Mo are incorporated from different sources. On the one hand, Mo incorporation from the mask and re-sputtering from the direct beam are equivalently proportional to J and, once the equilibrium conditions are reached, the Mo content is expected to remain constant with fluence. On the other hand, the Fe arrival pathway is due to the erosion of the cathodes immersed in the plasma discharge while Fe loss from the surface should be, as for Mo atoms, proportional to J. However, the increase in the rate of arrival of Fe on the target surface (measured by powering the ACC-IS without ion extraction, as described in [14]) with J is below unity (∼0.6). This scenario implies that the rate of erosion of Fe is promoted at higher J values, which explains the lower total metal content observed at 250 μA cm^{-2}. Apart from the average level of metals at both J values, the evolution with fluence is also different. Whereas at 250 μA cm^{-2} the metal content increases with fluence until attaining, within the experimental error, a constant level, it also increases initially at 50 μA cm^{-2} until a maximum value is reached for ion fluences close to 6×10^{17} ions cm^{-2}. For higher irradiation times, the measured metal content decreases slowly in such a way that for the longest time the metal content is $\sim 2.5 \times 10^{15}$ atoms cm^{-2} and a nanodot pattern morphology is formed. Since these changes of the irradiated surface metal content are correlated to the pattern change, it is not clear whether the nanohole structures are intrinsically stable or if their morphological evolution is governed by the dynamics of the metal content.

3.5. Compositional and chemical analysis of the irradiated surfaces by XPS and AES

The compositional RBS analysis shown in section 3.4 presents a depth resolution around 5–10 nm [29], which is of the order of the thickness of the surface amorphous layer originated by the ion damage (4–6 nm) [14]. Therefore, RBS analysis provides the total metal content averaged over the first few nanometres from the surface and cannot give resolved in-depth information regarding the metal distribution along this layer. Obviously, RBS is also not sensitive to the chemical state. In order to gain a deeper insight into these issues we have analysed by XPS and AES two samples patterned with nanohole and nanodot morphologies produced at low J conditions (50 μA cm^{-2}) for low (20 min) and high (210 min) sputtering times, respectively. Note that these two samples correspond to the extreme fluence values of the top curve in figure 8. Therefore this comparison aims at discerning differences in the pattern characteristics from both morphologies not directly related to the total metal content.

Figure 9 shows the XPS scans around the Si $2p_{3/2}$, Mo $3d_{5/2,3/2}$ and Fe $2p_{3/2}$ core levels in the nanohole (solid lines) and nanodot (dotted lines) structures before (bottom) and after (top) gentle Ar^+ ion beam surface cleaning. The data are presented without any background subtraction and only shifted vertically for comparison purposes. From the peak positions (see vertical lines as a guide), we can conclude that

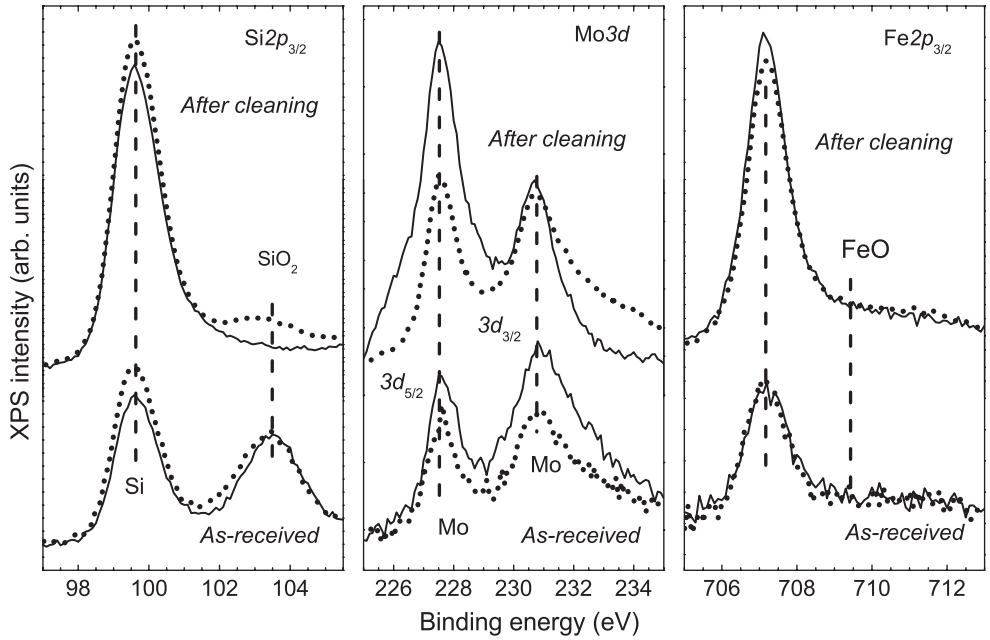

Figure 9. Si $2p_{3/2}$, Mo $3d_{5/2,3/2}$ and Fe $2p_{3/2}$ XPS spectra from samples with nanohole (solid lines) and nanodot (dotted lines) patterns. The scans recorded in the *as-received* samples (bottom curves) and *after cleaning* the surface with Ar^+ sputtering (top curves) are presented. The energy positions of some oxides are also indicated by vertical lines in the figure.

Table 1. Compositional analysis obtained from XPS, AES and RBS. XPS and AES values correspond to those measured after gentle Ar^+ cleaning. For computation of XPS and AES data, tabulated atomic sensitivity factors were used assuming a homogeneous metal distribution. For RBS data, we have considered the thickness of the amorphous silicon layer obtained from channelling measurements [14].

	XPS (at.%)		AES (at.%)		RBS (at.%)	
Sample	Nanohole	Nanodot	Nanohole	Nanodot	Nanohole	Nanodot
Fe	3.9 ± 0.2	4.0 ± 0.2	5.1 ± 0.7	4.7 ± 0.7	5.8 ± 0.6	5.0 ± 0.5
Mo	6.1 ± 0.2	2.4 ± 0.2	2.0 ± 0.3	1.7 ± 0.3	1.0 ± 0.1	1.3 ± 0.1
Total metal	10.0 ± 0.4	6.4 ± 0.4	7 ± 1	6 ± 1	6.8 ± 0.7	6.3 ± 0.6

Mo and Fe are in similar chemical states independently of the surface pattern. Further, the cleaning procedure does not alter the chemical state. However, note that the amount of Si, Mo and Fe increases after ion sputtering due to the removal of surface contamination (mainly, O and C). The latter can be mostly derived from the reduction of the SiO_2 contribution at the Si $2p_{3/2}$ peak after surface cleaning. We can also conclude that the formation of metal oxides is very low, negligible in the case of Fe (see the reduced intensity of Fe $2p_{3/2}$ at the position of Fe–O around 709.4 eV [23]) but more appreciable in the case of Mo. The presence of MoO_x is derived from several contributions within 229–232 eV [23] that increase the apparent intensity of the Mo $3d_{3/2}$ peak (see below). However, as in the case of SiO_2, this contribution is mostly reduced after sputter cleaning since the relative intensity of the Mo $3d_{3/2}$ and Mo $3d_{5/2}$ is similar to that of pure Mo [30]. The previous results confirm that metal and silicon oxides are partially or completely removed after erosion of a few surface layers with ion cleaning, indicating that the oxidation is restricted to the near surface regions and, hence, produced by air exposure after preparation.

For comparison, table 1 gathers the atomic concentrations derived from XPS and AES after ion cleaning, together with those obtained from RBS. Taking into account the different depth resolutions, sampling areas, data errors and the surface cleaning before XPS and AES measurements, the three techniques yield similar values. For example, the Mo concentration obtained by XPS for the nanohole pattern is higher, although this difference could be accounted for by the quite larger sampling area of XPS ($\sim$1 cm^2) compared to that of AES (spot $\sim$0.1 mm wide) and considering that Mo incorporation increases in the region closer to the Mo mask. Also, XPS and AES analysis yield a metal content at the near surface region between 5 and 10 at.%. This range is in agreement with the RBS data and, noticeably, with the AES data reported by Ozaydin *et al* [12]. This means that metals are not constrained to the surface and are mostly distributed within the 4–6 nm amorphous layer.

Another interesting observation is that RBS tends to give slightly higher (lower) Fe (Mo) concentration values than XPS and AES for both patterns. It is worth mentioning that preferential sputtering of Fe after cleaning could affect the obtained AES and XPS values. However, this difference can be also explained by an inhomogeneous in-depth distribution of Fe and Mo. This may be expected as a result of the different sputtering yields of each element site, in analogy with the evolution of the surface composition during sputtering of alloys [31]. This possibility is supported by the AES depth

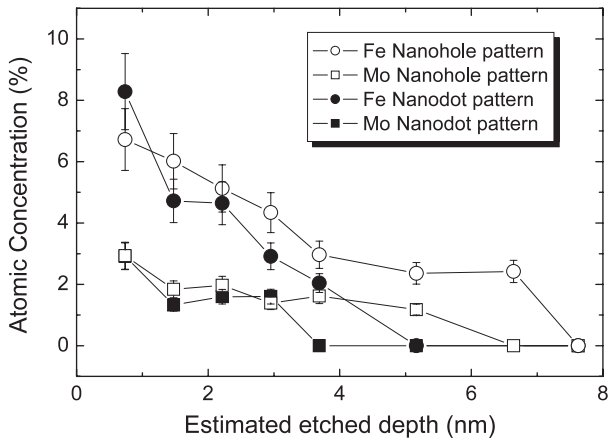

Figure 10. AES compositional profiles for nanodot and nanohole patterns. Note the higher metal content in the nanodot pattern and the deeper Fe distribution than in the case of Mo.

profile shown in figure 10. It should be mentioned that the absolute depth values derived from AES are only indicative since they have been calculated by assuming the erosion rate of bare Si. First, in concordance with table 1, the profiles show that the total metal content (extracted from the profile integral) is higher in nanohole patterns than in nanodots. Besides, it is clearly observed that, for both patterns, Mo atoms have a shallower depth distribution than in the case of Fe. This fact is consistent with the observed underestimation (overestimation) of Mo (Fe) by RBS (table 1). Another interesting feature in figure 10 is the slightly, but still appreciable, larger thickness of the metal-containing layer for the sample with nanohole structures. In fact, this would be the main difference between nanohole and nanodot patterns besides the slightly higher total metal content in the nanohole pattern. This result cannot be related to the ion induced amorphous layer, since the ion range is equivalent in both cases, but could be affected to some extent by eventual artefacts related to the depth profiling process, performed at an angle of 55° with respect to the normal to the surface, on different initial sample morphologies. Also, preferential sputtering could play a role in the measured metal depth distribution.

As a final remark in this section, the formation of silicides has been verified by high-resolution XPS. As shown in figure 11, the chemical shift due to silicide bonds is found to be ∼0.4 and 0.3 eV for the Mo 3d and Fe $2p_{3/2}$ peaks, respectively. This has been directly obtained from the comparison with reference spectra of Mo and Fe foils (measured in the same run and after ion surface cleaning to remove surface contamination). For the Mo foil, note the contribution from Mo–O bonds in the as-received spectrum (dotted line) at ∼229 and ∼232 eV, in line with the observations discussed previously. Although the chemical state around Mo and Fe cannot be related to the nanohole and nanodot selection (see figure 9), this is the first clear evidence of silicide formation in IBS nanopatterns. The eventual implications of a such finding in the nanostructuring process are briefly discussed in section 4.

4. Summary and outlook

4.1. Exploring other IBS configurations for nanohole pattern production

From the data shown in section 3, it has been concluded that there is a correlation between the metal content and the surface pattern morphology. However, whether or not the formation of nanoholes is exclusively related to the ACC-IS is not clear. This issue is related to the universality of IBS

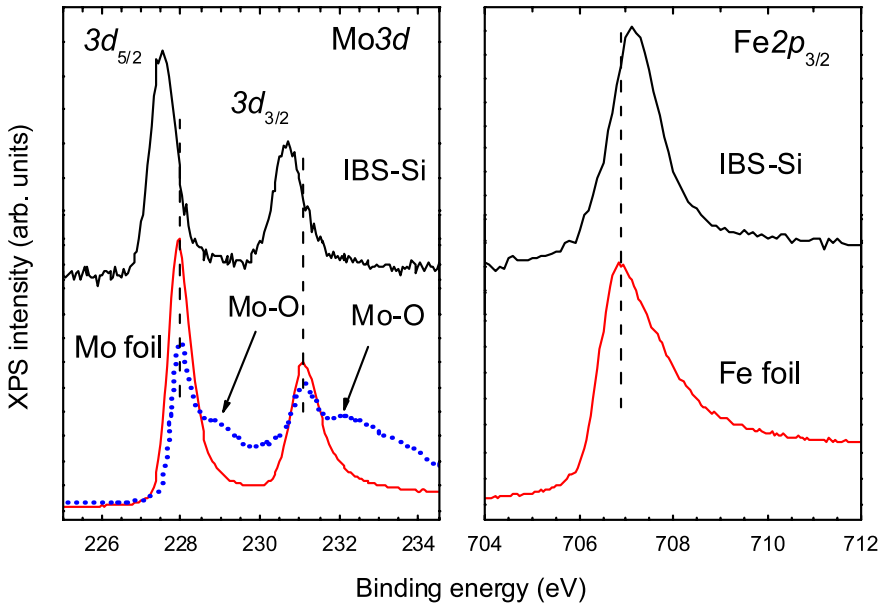

Figure 11. High-resolution XPS spectra of Mo 3d and Fe $2p_{3/2}$ core levels from a sample with a nanohole pattern (top spectra) and pure metal foils (bottom spectra). In both cases, the peak positions, as compared to pure metal references (vertical dashed lines in bottom spectra), evidence a chemical shift due to the formation of metal silicides. For the Mo foil sample, the spectra obtained before (dotted line) and after (solid line) the cleaning process are shown.

patterning given in section 1 and the (possible) influence of the specific experimental set-up. As indicated above, this ACC-IS presents an unavoidable flux of Fe from the cathodes towards the target. A drawback of this configuration is that the fluxes of Fe and ions extracted from the ion source are correlated. In order to get a deeper understanding of the effect of metal incorporation and using the knowledge acquired with the ACC-IS system, we have also explored the eventual formation of nanohole patterns with other ion sources. In particular, we have used the more standard Kaufman type in which, in contrast to the ACC-IS, a filament is used to ignite the plasma discharge. Under this configuration, the flux of Fe atoms from the source is suppressed. Here, we present preliminary results on nanohole pattern formation on Si(001) targets with a Kaufman ion gun and simultaneous metal (Fe and Mo) incorporation. According to the conditions reported for nanohole production with the ACC-IS, we have irradiated Si(001) targets for low $J(<50\ \mu\text{A cm}^{-2})$ and fluences $((3–5)\times 10^{17}\ \text{ions cm}^{-2})$. Also, we have searched for a target mask configuration which yields similar Fe and Mo levels as those found with the ACC-IS by reducing the inner hole diameter of a Fe mask (10 mm) and sticking Mo stripes on the outer part.

The nanohole pattern produced with a Kaufman-type ion source is shown in figure 12. As shown in the inset, these structures displayed short-range hexagonal order similar to the nanohole patterns produced with the ACC-IS system (figure 1(b)). In figure 12(b) we also show a typical PSD function of one of these nanohole structured surfaces with a clear peak, associated with the average hole–hole distance of $\lambda \sim 49$ nm. In this case, the total metal content measured by RBS for the nanohole structures produced with the Kaufman source configuration was in the $(3.5–5)\times 10^{15}$atoms cm^{-2} range whereas nanodot surfaces displayed metal contents below the $\sim 3.3\times 10^{15}$ atoms cm^{-2} range. This result confirms the overall trend reported in section 3 and in [14], where nanohole formation takes place for higher metal contents than in the case of nanodots. More systematic experiments are in progress in order to confine the range of metal content associated with nanohole patterns in the Kaufman system. Also, other experiments will be carried out in order to sample the IBS parameter window for the formation of nanohole/nanodot structures and their correlation with metal incorporation. In fact, IBS with the Kaufman ion gun allows us to design more controlled experiments in order to better determine the role of simultaneous metal incorporation in the resulting IBS induced surface patterns. In particular, it will be interesting to analyse the dynamics with ion fluence of the nanohole structures produced with the Kaufman system. This study would contribute to elucidating the source of the instability linked to the nanohole patterns.

Regarding other open questions to be addressed, one should determine the need for several metal sources for nanohole production. For example, nanodot patterns have been reported with either Mo [12], Fe [10, 27] or Fe/Mo [14] impurities, suggesting that, for this morphology, the nature of the metal is not so critical. Also, in the case of Fe and Mo incorporation, although the Fe/Mo ratio does not seem to be a critical point in the nanohole production (figure 7), some

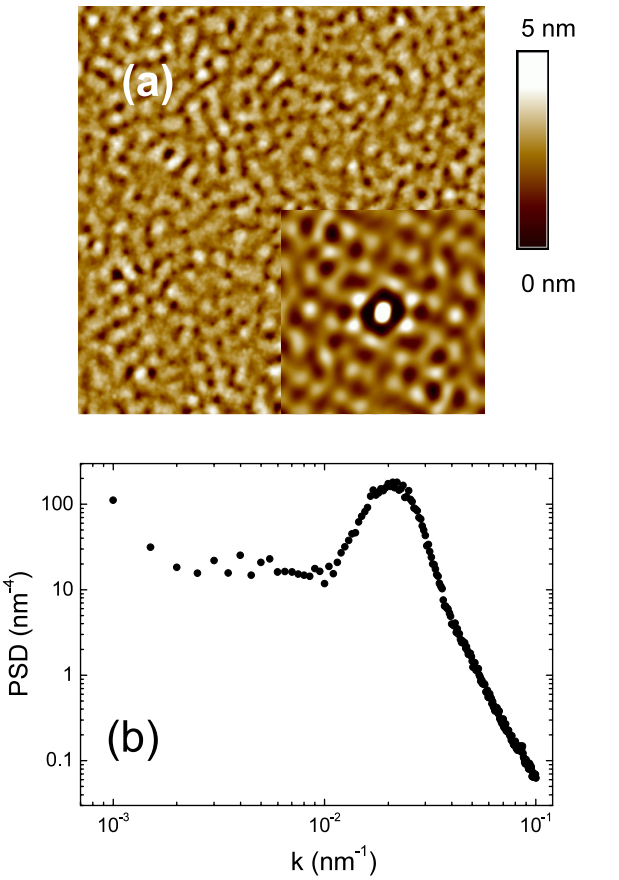

Figure 12. (a) $2\times 2\ \mu\text{m}^2$ AFM image showing the morphology of a Si(001) surface irradiated under normal incidence by 1 keV Ar^+ ion beam for an ion flux of 55 μA cm^{-2} and an ion fluence of 4×10^{17} ions cm^{-2} extracted from a Kaufman ion gun as described in the text. The inset in figure (a) shows the autocorrelation function taken on a 400×400 nm^2 region. (b) PSD function of the image shown in (a).

findings suggest that this value, or at least their arrival/loss rates at the target surface, can affect the nanohole parameter window (in terms of J and fluence). Other binary metal combinations could yield some more data, especially for species with very different sputtering yields. Finally, all the previous experiments rely on an indirect metal source (masks, clamps, source cathodes, ...), where the incoming metal flux toward the target is correlated with other process parameters such as the ion flux. Therefore, it would be desirable to design experiments with appropriate set-ups where the metal and ion fluxes have independent sources.

4.2. The possible mechanisms induced by metal incorporation during IBS

The experimental conditions and evidence reported here for nanohole production do not provide solid conclusions on the mechanisms ruling such pattern formation. This is partially due to the complex experimental system where many parameters are interrelated and to the dynamical character of the process. Theoretically, the formation of nanohole or nanodot patterns by IBS has been predicted [32], where the

morphology is selected by the ratio between the ion range (a) and the longitudinal (σ) and lateral (μ) straggling. As derived from TRIM simulations [14], the surface metal-containing layer can modify the values of a, σ and μ. However, these simulations do not provide reliable absolute values of σ and μ [33] and the dynamical process of simultaneous metal supply during IBS cannot be incorporated into the simulations. In addition, the scenario can become quite complex since multiple phenomena could operate simultaneously. For example, we can mention the following:

(i) One important parameter to be taken into account is the eventual increase in surface temperature during the IBS process. This could cause radiation-enhanced diffusion (RED) effects, and therefore induce an inhomogeneous metal concentration on the surface, as reported for ion bombarded bulk alloys [34]. However, the studies presented in this work addressing the influence of the target temperature on the nanohole pattern morphology indicate that nanohole patterns disappear for $T > 350$ K. Therefore, RED effects can be, in principle, neglected.

(ii) The stress generated in the near surface region by low-energy ion bombardment can also play a crucial role in the stability of IBS patterned nanostructures [35]. The characterization of surface stress during IBS nanopatterning has begun to be addressed both theoretically and experimentally [35–37]. In fact, it has recently been proposed that tensile stress can play a dominant role in driving the nanodot production on Si surfaces during normal incidence Ar^+ ion bombardment with simultaneous Mo incorporation [24]. Therefore, the modification of surface stress fields by metal incorporation could be responsible for the selective production of nanohole and nanodot patterns reported here.

(iii) Another mechanism that can be relevant during IBS with simultaneous metal incorporation is the ion induced formation of chemical heterogeneities on the surface. From the compositional analysis, it has been shown that a few at.% of Mo and Fe are incorporated on the silicon surface. These metal atoms are highly reactive with Si and the formation of a silicide layer has been corroborated here. This scenario is somehow akin to that considered for IBS patterning of alloy surfaces [13]. In that study, it was predicted that elements with different sputter yields and surface diffusivities within the alloy constituents would lead to spontaneous composition modulations correlated with the surface topography. In principle, this possibility cannot be discarded in our case since we have found a clear correlation between the total metal content and the pattern morphology. Moreover, it is evident that the surface chemical heterogeneity introduced by silicide formation would result in local changes of the sputtering yield or, as discussed, in the shape of the collision cascade. Finally, processes like those taking place during IBS of multi-component bulk targets, such as preferential sputtering effects and Gibbsean segregation [31], cannot be ruled out. However, in our case the scenario seems to be more complicated than in a multi-component bulk target since our system consists of a ∼5 nm thick Si–Fe–Mo layer on top of silicon bulk. In order to assess this unambiguously, it would be necessary to realize simultaneously chemical and morphological characterizations with nanometre lateral resolution. Such investigations are being envisaged for the near future.

(iv) Other possible contribution to nanohole/nanodot production could arise from the well known supply of 'seed' materials for target nanostructuring by IBS [38]. In general, impurities with either a lower sputtering yield [39], such as Mo, or a higher melting point than the target constituents [40] behave as seeds. In our case, the seeding process could also be linked to silicide formation. Typically, nanocone structures, aligned along the ion beam direction, are usually formed on the seeded surface after irradiation. In this process, seed and target atom migration seems to play an important role [39]. In fact, it has been reported [39] that Mo-seeded silicon nanorods become narrower and longer (i.e. higher) and more densely packed with increasing target temperature. However, the influence of the target temperature on the pattern morphology by IBS is not clear enough to confirm this 'seeding' scenario. We have observed that λ decreases with T (figure 6(b)) in agreement with seeding experiments. However, w, which is mainly determined by the height of the nanostructure, initially does increase slightly, which would agree with Mo-seeding experiments, but decreases for $T > 450$ K. It is interesting to note that for our previous study [27] of nanodot pattern dependence on temperature, where unintentional Fe incorporation took place [14], λ and w did decrease for increasing T. These findings are, to some extent, contradictory since the decrease of surface roughness is consistent with thermally induced surface relaxation mechanisms [27] but not with Mo-seeding experiments [39]. On the contrary, the decrease of λ with T agrees with the behaviour found for Mo-seeding IBS but not with the behaviour expected when thermally activated surface relaxation processes determine the surface morphology. These results suggest that thermal diffusion and seeding may compete, being dominant for different T ranges.

In summary, it is clear that further investigations are required for a deeper understanding of the nanostructuring process by IBS under simultaneous metal incorporation. Both experimental and theoretical efforts should be made to discriminate the eventual participation of the mechanisms mentioned above or to identify additional ones. All these issues remain to be addressed in future work.

5. Conclusions

In conclusion, we have reported the successful surface nanostructuring of Si(001) surfaces with an ACC-IS source, where Fe and Mo impurities are incorporated during IBS. Under these conditions, nanohole patterns are produced for low ion fluxes (<100 μA cm^{-2}) and relatively low ion fluences ($<10^{18}$ ions cm^{-2}), whereas nanodot morphologies are produced above this window. Therefore, nanohole morphologies are obtained in a narrow IBS window and, contrary to the nanodot case, the pattern is not stable under long time irradiation. RBS compositional analysis has shown that nanohole morphologies are produced when the metal content on the irradiated surfaces is higher (within $(2.5–3.5) \times 10^{15}$ atoms cm^{-2}) than in the case of nanodots ($<2.5 \times 10^{15}$ atoms cm^{-2}).

The role of metal incorporation on the pattern selectivity has been corroborated qualitatively by extending the results obtained with the ACC-IS to a 'cleaner' Kaufman-type ion source. In order to gain some information on the metal effects, chemical analysis of the surface has been performed to complement the compositional RBS results, showing for the first time the dominant participation of metal silicides. The future outlook and a discussion regarding the role of metal incorporation have also been given.

Acknowledgments

We are thankful to R Cuerno, J Muñoz-García and M Castro for helpful discussions and suggestions and to C Rogero for her assistance in XPS measurements and data processing. This work has been partially supported by grants FIS2006-12253-C06-02 (MEC, Spain), FIS2006-12253-C06-02-03 (MEC, Spain), CCG08-CSIC/MAT-3457 (CAM, Spain), S-505/AMB/259 (CAM, Spain) and Consolider-Ingenio CSD2007-00010 and CSD2008-00023 (MEC, Spain). High-resolution XPS measurements were made with financial support of the MEC/CSIC grant CSIC-05-33-086. JAS-G acknowledges financial support from the I3P programme (CSIC, Spain).

References

[1] Muñoz-García J, Vázquez L, Cuerno R, Sánchez-García J A, Castro M and Gago R 2009 Self-organized surface nanopatterning by ion beam sputtering *Lecture Notes on Nanoscale Science and Technology* ed Z Wang (Berlin: Springer) (arXiv:0706.2625)
[2] Valbusa U, Boragno C and Buatier de Mongeot F 2002 *J. Phys.: Condens. Matter* **14** 8153
[3] Carter G 2001 *J. Phys. D: Appl. Phys.* **34** R1
[4] Chan W L and Chason E 2007 *J. Appl. Phys.* **101** 121301
[5] Castro M, Cuerno R, Vázquez L and Gago R 2005 *Phys. Rev. Lett.* **94** 016102
Muñoz-García J, Castro M and Cuerno R 2006 *Phys. Rev. Lett.* **96** 086101
[6] Ziberi B, Frost F, Tartz M, Neumann H and Rauschenbach B 2004 *Thin Solid Films* **459** 106
[7] Cuenat A and Aziz M J 2002 *Mater. Res. Soc. Symp. Proc.* **696** N2.8.1
[8] Madi C S, George H B and Aziz M J 2009 *J. Phys.: Condens. Matter* **21** 224010
[9] Facsko S, Dekorsy T, Koerdt C, Trappe C, Kurz H, Vogt A and Hartnagel H L 1999 *Science* **285** 1551
[10] Gago R, Vázquez L, Cuerno R, Varela M, Ballesteros C and Albella J M 2001 *Appl. Phys. Lett.* **78** 3316
Gago R, Vázquez L, Cuerno R, Varela M, Ballesteros C and Albella J M 2002 *Nanotechnology* **13** 304
[11] Ziberi B, Frost F and Rauschenbach B 2006 *Appl. Phys. Lett.* **88** 173115
[12] Ozaydin G, Özcan A S, Wang Y, Ludwig K F, Zhou H, Headrick R L and Siddons D P 2005 *Appl. Phys. Lett.* **87** 163104
[13] Shenoy V B, Chan W L and Chason E 2007 *Phys. Rev. Lett.* **98** 256101
[14] Sánchez-García J A, Vázquez L, Gago R, Redondo-Cubero A, Albella J M and Czigány Zs 2008 *Nanotechnology* **19** 355306
[15] http://www.jenion.de
[16] Zhong Z, Halilovic A, Fromherz T, Schäffler F and Bauer G 2003 *Appl. Phys. Lett.* **82** 4779
[17] Karmous A, Cuenat A, Ronda A, Berbezier I, Atha S and Hull R 2004 *Appl. Phys. Lett.* **85** 6401
[18] Liang J, Hong S K, Kouklin N, Beresford R and Xu J M 2003 *Appl. Phys. Lett.* **83** 1752
[19] Yoon T S, Zhao Z, Liu J, Xie Y H, Ryu D, Russell T P, Kim H M and Kim K B 2006 *Appl. Phys. Lett.* **89** 063107
[20] Lagally M G and Blick R H 2004 *Nature* **432** 450
[21] Shchukin V A and Bimberg D 1999 *Rev. Mod. Phys.* **71** 1125
[22] Tsamouras D, Palasantzas G and De Hosson J Th M 2001 *Appl. Phys. Lett.* **79** 1801
[23] Briggs D and Seah M P 1990 *Practical Surface Analysis* 2nd edn, vol 1 (New York: Wiley)
[24] Ozaydin G, Ludwig K F, Zhou H and Headrick R L 2008 *J. Vac. Sci. Technol.* B **26** 551
[25] Gago R, Vázquez L, Plantevin O, Metzger T H, Muñoz-García J, Cuerno R and Castro M 2006 *Appl. Phys. Lett.* **89** 233101
[26] Muñoz-García J *et al* 2009 in preparation
[27] Gago R, Vázquez L, Sánchez-García J A, Varela M, Ballesteros M C, Plantevin O, Albella J M and Metzger T H 2006 *Phys. Rev.* B **73** 0155414
[28] Barabási A L and Stanley H E 1995 *Fractal Concepts in Surface Growth* (Cambridge: Cambridge University Press)
[29] Chu W K, Mayer J W and Nicholet M A 1978 *Backscattering Spectrometry* (New York: Academic)
[30] Wagner C D, Riggs W M, Davis L E and Moulder J F 1979 *Handbook of X-Ray Photoelectron Spectroscopy* (Eden Prairie, MN: Physical Electronics Division, Perkin-Elmer Corporation)
[31] Zaporozchenko V I and Stepanova M G 1995 *Prog. Surf. Sci.* **2** 155
[32] Kahng B, Jeong H and Barabási A L 2001 *Appl. Phys. Lett.* **78** 80
[33] Bobek T, Facsko S, Kurz H, Dekorsy T, Xu M and Teichert C 2003 *Phys. Rev.* B **68** 085324
[34] Lam N Q, Tang S, Yacout A M, Rehn L-E and Stubbins J F 1991 *Nucl. Instrum. Methods* B **59/60** 889
[35] Chan W L and Chason E 2008 *J. Vac. Sci. Technol.* A **26** 44
[36] Kalyanasundaram N, Moore M C, Freund J B and Jonson H T 2006 *Acta Mater.* **54** 483
[37] Dahmen K, Giesen M, Ikonomov J, Starbova K and Ibach H 2003 *Thin Solid Films* **428** 6
[38] Tanemura M, Yamauchi H, Yamane Y, Okita T and Tanemura S 2004 *Nucl. Instrum. Methods* B **215** 137
[39] Tanemura M, Kobayashi M, Kudo M, Yamauchi H, Okita T, Miao L and Tanemura S 2006 *Surf. Sci.* **600** 3668
[40] Wehner G K 1985 *J. Vac. Sci. Technol.* A **3** 1281